AIAA 98-3699

Characterization of the Laminar Boundary Layer in Solid Rocket Motors

J. Majdalani
Marquette University
Milwaukee, WI 53233

34th AIAA/ASME/SAE/ASEE Joint Propulsion Conference & Exhibit
July 13–15, 1998 / Cleveland, OH

For permission to copy or republish, contact the American Institute of Aeronautics and Astronautics
1801 Alexander Bell Drive, Suite 500, Reston, Virginia 20191-4344

CHARACTERIZATION OF THE LAMINAR BOUNDARY LAYER IN SOLID ROCKET MOTORS

J. Majdalani*
Marquette University, Milwaukee, WI 53233

Abstract

This paper investigates the structure of the boundary layer in cylindrical rocket motors in light of two recent analytical solutions to the time-dependent axisymmetric flowfield that have been shown to agree with numerical and experimental predictions in the forward portions of the motor where the flow remains laminar. To that end, closed form expressions that define the character of the oscillatory boundary layer are obtained in order to bring physical details into focus. The short flowfield solution published recently (Majdalani, J., and Van Moorhem, W.K., "Improved Time-Dependent Flowfield Solution for Solid Rocket Motors," *AIAA Journal*, Vol. 36, No. 2, 1998, pp. 241-248) makes it possible to arrive at analytical expressions that elucidate the intricate features of the boundary-layer zone; the latter is found to encompass a relatively large portion of the combustion chamber in most rockets for low acoustic modes. The depth of penetration is found to depend on the size of the penetration number, the acoustic mode, and the distance from the head-end. An assessment of the location and size of the Richardson overshoot is also pursued. Closed form expressions are provided for the penetration depth, speed of propagation, wavelength, amplitude and phase relation between unsteady velocity and pressure components. Increasing viscosity is found to reduce the size of the rotational region. By comparison to the acoustic boundary layer assumed in one-dimensional acoustic theory, the actual character of the rotational region is quite dissimilar. Finally, analytical results are verified numerically against a modern and reliable, compressible Navier-Stokes solver.

*Assistant Professor, Department of Mechanical and Industrial Engineering. Member AIAA.
Copyright © 1998 by J. Majdalani. Published by the American Institute of Aeronautics and Astronautics, Inc., with permission.

Nomenclature

a_0	= stagnation speed of sound, $\sqrt{\gamma p_0 / \rho_0}$
f_m	= dimensional frequency for mode m, Hz
k_m	= wave number, $m\pi R / L = \omega_0 R / a_0$
L	= internal chamber length
M_b	= wall injection Mach number, V_b / a_0
p_0	= mean chamber pressure, $\rho_0 a_0^2 / \gamma$
p	= dimensionless pressure, p^* / p_0
r	= radial position, $r^* / R = (1-y)$
R	= dimensional effective radius
Re_k	= kinetic Reynolds number, $\omega_0 R^2 / \nu_0$
Sr	= Strouhal number, $\omega_0 R / V_b = k_m / M_b$
t	= dimensionless time, $t^* a_0 / R$
U_r	= radial mean flow velocity, $-r^{-1} \sin\theta$
$u^{(1)}$	= total unsteady velocity, $u^{*(1)} / a_0$
V_b	= radial injection speed at the wall
y	= distance from the wall, $y^* / R = (1-r)$
z	= axial distance from the head-end, z^* / R
ε_w	= normalized pressure wave amplitude
γ	= mean ratio of specific heats
λ	= spatial wavelength of rotational waves
ν_0	= chamber fluid mean kinematic viscosity
θ	= characteristic variable, $\pi r^2 / 2$
ρ_0	= chamber mean density
ω_m	= dimensionless frequency, $m\pi R / L$
ω_0	= dimensional frequency, $m\pi a_0 / L$
ξ	= viscous parameter, $S_p^{-1} = \omega_0^2 \nu_0 R / V_b^3$

Subscripts

m	= refers to a maximum or a mode number
p	= refers to a depth of penetration
w	= refers to the wall
b	= refers to blowing or burning at the wall

Superscripts

*	= asterisk denotes a dimensional quantity
~	= tilde denotes vortical oscillations

Introduction

In recent years, the boundary-layer structure in solid rocket motors has received much attention in the rocket combustion stability community. This might be attributed to the important role that it plays in understanding a number of combustion mechanisms that occur in the vicinity of the burning surface. Since understanding the structure of the boundary layer can help understand pressure coupling, velocity coupling, transition to turbulence, and the flame zone interaction with the internal flowfield, several researchers have undertaken analytical,[1-9] numerical,[10-19] and experimental investigations[20-21] aimed at elucidating intricate field interactions near the propellant surface.

The main focus of this paper will be to analyze the boundary-layer structure resulting from two recent analytical models for the flowfield that have been shown to agree very favorably with available numerical and experimental data.[3] The first model was derived by Flandro[7] using the vorticity transport equation and regular perturbations. The second was derived by Majdalani and Van Moorhem[2-3] using a novel, composite-scale perturbation technique. Both models have been shown recently to concur over a large range of physical parameters despite their dissimilar analytical formulations. One appealing feature of the composite-scale model[3] is that it offers a short expression for the velocity field which allows extracting information about the boundary layer in closed analytical form. The current paper will exploit this feature to elucidate the character of the oscillatory boundary layer and explain the influence of various flow variables on its structure. In the process, several related issues will be addressed individually. These include the boundary-layer thickness or penetration depth of the rotational region, the peculiar Richardson overshoot,[22] the spatial wavelength and speed of propagation, and the controversial phase difference between oscillatory pressure and velocity. Since the present analysis is only applicable to laminar fields, it is hoped that the information provided here will be used in developing a working analytical theory for turbulence, which recent work by Yang and co-workers has shown to appear in the aft portion of the rocket chamber.[23] Finally, analytical results are further validated through comparisons drawn against reliable computational data acquired from a modern Navier-Stokes solver developed by Roh and co-workers.[23]

Analysis

Wave Characteristics

Using the exact same notation as previously, the current analysis begins by considering the total time-dependent velocity obtained from Ref. 3 [Eq. (63)], which is known to the order of the Mach number:

$$u^{(1)}(r,z,t)=\frac{\varepsilon_w}{\gamma}\Bigg[\overbrace{\sin(k_m z)\sin(k_m t)}^{\text{Irrotational part}} \overbrace{-\underbrace{\sin\theta\sin(k_m z\sin\theta)\exp\zeta}_{\text{Wave amplitude}}\underbrace{\sin(k_m t+\Phi)}_{\text{Propagation}}}^{\text{Rotational part}}\Bigg] \tag{1}$$

where

$$\zeta(r)=\xi\eta(r)r^3\csc^3\theta,\quad \Phi(r)=\frac{Sr}{\pi}\ln\tan\frac{\theta}{2} \tag{1a}$$

and

$$\eta(r)=-y\left[1+cy^c\left(yr^{-1}-c\ln r\right)\right]^{-1},\ c=3/2 \tag{1b}$$

The radial velocity component has been deliberately ignored in Eq. (1), being smaller in magnitude than the axial component. The total time-dependent velocity consists of a linear juxtaposition of inviscid-acoustic-irrotational and viscous-solenoidal-rotational fields. The rotational component represents a harmonic wave traveling radially toward the centerline; this wave suffers from exponential damping with increasing distance from the wall. From Eq. (1) it can be inferred that the vortical wave amplitude is controlled by two terms: 1) an exponentially decaying term (made possible by inclusion of viscous effects) that diminishes with increasing distance from the wall, and 2) a sinusoidal term (made possible by inclusion of downstream convection of unsteady vorticity by the mean flow) which, in addition to its monotonic decrease with increasing distance from the wall, varies harmonically with the distance from the head-end. Since the exponentially decaying wave amplitude term depends directly on $\xi = \omega_0^2 \nu_0 R / V_b^3$, it is clear that large viscosity causes the amplitude to decay more rapidly. Viscosity is hence identified to be an attenuation factor whose role is to impede the inward penetration of vorticity.

Equation 1 also indicates that the axial variation in the wave amplitude along the centerline is controlled exclusively by the acoustic field, while the radial variation is prescribed by the rotational field which plays a crucial role in the accurate assessment of the boundary layer envelope. On a separate note, recalling that the phase of the rotational wave is uniform along lines where $(k_m t + \Phi)$ is constant, Eq. (1) allows solving for the radial speed of wave propagation which is determined to be equal to Culick's radial mean flow velocity.[24] This reassuring result is evidence that the solution exhibits the correct coupling between mean and time-dependent elements and that the time-dependent field is indeed driven by the mean flow. More details are furnished below.

Unsteady Axial Velocity Profile

Results from the regular perturbation solution by Flandro[7] and the composite-scale technique (CST)[3] are found to concur substantially with the numerical solution which is achieved with a high order of accuracy (using a 9-stage Runge-Kutta scheme, and a step size of 10^{-6}, with an associated global error of order seven).[25] It follows that the agreement between analytical and numerical predictions is so remarkable that graphical results are visually undiscernible. The periodic velocity distribution at evenly spaced times is shown in Fig. 1, for one full cycle of oscillations, and for the first four acoustic oscillation modes. The control parameters are chosen from typical values associated with a tactical rocket motor, as classified by Flandro ($Sr = 51m$, $Re_k = 2.1m\text{x}10^6$ from Table 1 in Ref. 7). The profiles are displayed at the axial position corresponding to the location from the head-end of the first (Figs. 1a-d) and last (Figs. 1e-g) acoustic velocity antinode. A key feature captured remarkably by the analytical solution is that of the rotational velocity amplitude vanishing m times at the m^{th} velocity antinode. As shown in Figs. 1e-g, the rotational amplitude decays prematurely to zero somewhere between the wall and the centerline corresponding to lines of zero unsteady vorticity. This peculiar effect, which is attributable to the downstream convection of zero unsteady vorticity lines by Culick's mean flow,[24] is further evidence that the influence of the mean flow on the time-dependent field has been correctly incorporated.

Boundary Layer Thickness or Penetration Depth

In recognition of the fact that both regular perturbation and CST models exhibit similar velocity profiles, their penetration depths are expected to be similar as well. A typical comparison obtained from the aforementioned models is drawn in Fig. 2 at two axial locations, for a large range of dynamic similarity parameters, Sr and Re_k. Remarkably, the entire family of curves shown in Fig. 2 collapses into a single curve per axial location, when plotted versus the penetration number, $S_p = \xi^{-1}$, revealed by the analytical derivation. This appealing discovery allows us to represent the complete solution for the boundary-layer thickness on one single graph per oscillation mode. As shown in Fig. 3, characteristic curves of penetration depths at several axial locations spanning the length of the chamber are conveniently depicted for the fundamental oscillation mode. Having collapsed the results onto a single graph provides numerous advantages, including concrete means to explain and interpret the boundary layer structure.

As could be inferred from Fig. 3, the dependence of the penetration depth on the axial location z is minute in the forward half of the chamber, and becomes more pronounced in the aft half. The increased sensitivity of the boundary layer thickness to z with increasing axial distance from the head-end is attributed to vortical intensification in the streamwise direction. For first mode oscillations, the axial dependence is found to be only important in the aft-half of the chamber, when z becomes relatively large. For a range of penetration numbers, the depth of penetration is found to be dependent only on the penetration number and, to a lesser extent, on the axial location. For small penetration numbers, the penetration depth is found to be directly proportional to the penetration number, independently of the axial location. This takes place when the mean flow injection speed is very small, resulting in insignificant vortical intensification in the streamwise direction. Evidently, this range does not correspond to rockets characterized by sizeable penetration numbers and relatively large penetration depths, especially for fundamental oscillatory modes.

The sensitivity of the penetration depth to variations in the penetration number decreases at higher values of the penetration number corresponding to frictionless flows. As the penetration number becomes large, say exceeding 100, the value of the penetration depth becomes independent of the penetration number, and can be estimated from an asymptotic solution to the inviscid formulation. This maximum possible penetration depth y_{pm} that can occur at any axial location is shown in Fig. 4 for the first four oscillation modes. Clearly, the maximum penetration depth increases with the axial location and the mode number. The axial increase is not monotone, since y_{pm} reaches a maximum at the acoustic velocity nodes where the boundary layer fills the entire chamber. The numerical and analytical results shown in Fig. 4 are obtained from Eq. (4) and Eq. (5), respectively. These equations are derived below.

Boundary-Layer Envelope

The outer envelope of the time-dependent boundary layer depends on the rate of decay of the wave amplitude. From Eq. (1), the wave amplitude that controls the evolution of the outer envelope of the rotational velocity is easily recognized to be

$$\|\tilde{u}^{(1)}\| = \frac{\varepsilon_w}{\gamma}\sin\theta\sin(k_m z\sin\theta)\exp\left(\frac{\eta}{S_p}r^3\csc^3\theta\right) \quad (2)$$

The point directly above the wall where this amplitude reaches 1% of its irrotational counterpart in Eq. (1) defines the edge of the boundary layer. In this case, the point must be calculated by finding the root r_p of

$$\sin\left(\frac{\pi}{2}r_p{}^2\right)\sin\left[k_m z\sin\left(\frac{\pi}{2}r_p{}^2\right)\right] \times\exp\left[\frac{\eta(r_p)}{S_p}r_p{}^3\csc^3\left(\frac{\pi}{2}r_p{}^2\right)\right]-\alpha\left|\sin(k_m z)\right|=0 \quad (3)$$

where $\alpha = 0.01$ defines the 99% based boundary-layer thickness. In general, this penetration depth will depend on the penetration number, the mode number, and the axial location in the chamber. The larger the penetration number, the larger the penetration depth will be due to a smaller argument in the exponentially decaying term arising in Eq. (3). This establishes the role of viscosity, discussed earlier, as an agent that attenuates the strength and penetration of vortical waves. Obviously, the smaller the viscosity, the larger the penetration depth will be. The upper limit on the boundary-layer thickness can therefore be determined from the inviscid formulation of the penetration depth. Setting the viscosity equal to zero in Eq. (3), the maximum penetration depth is found to be a sole function of the axial location and mode numbers:

$$\sin\left(\frac{\pi}{2}r_{pm}{}^2\right)\sin\left[k_m z\sin\left(\frac{\pi}{2}r_{pm}{}^2\right)\right]-\alpha\left|\sin(k_m z)\right|=0 \quad (4)$$

Inviscid Boundary-Layer Envelope

Equation (4) can be manipulated algebraically to reveal a closed form asymptotic expansion for the maximum penetration depth. This is made possible by taking advantage of the fact that r_{pm} is smaller than unity. The 99% inviscid thickness can be evaluated either numerically or from a one-term expansion of order $r_{pm}{}^6$, extracted from Eq. (4). This expansion formula is

$$y_{pm} = 1-\left[\frac{4}{\pi^2}\alpha\frac{\left|\sin(k_m z)\right|}{k_m z}\right]^{1/4}+O\left(r_{pm}{}^6\right) \quad (5)$$

Since the minimum possible y_{pm} is 74.8% at $z = 0$, r_{pm} cannot exceed a value of 0.252. The maximum error associated with Eq. (5) can hence be calculated to be 0.000259, which is an order of magnitude smaller than the Mach number. This maximum error can only affect the depth of penetration in the third or fourth decimal places, a practically negligible contribution, which also explains the excellent agreement in Fig. 4 between analytical and numerical predictions.

Unsteady Velocity Overshoot

The phase difference between rotational and irrotational solutions causes a periodic overshoot of the total velocity that can reach almost twice the irrotational wave amplitude. This overshoot is a well known effect that is characteristic of oscillatory flows. It was first discovered in experiments on sound waves in resonators by Richardson[22] who first realized that maximum velocities occurred in the vicinity of the wall. Theoretical verifications of this peculiar phenomenon were carried out by Sexl,[26] and additional confirmatory experiments were conducted by Richardson and Tyler[27] on reciprocating flows subject to pure periodic motions without mean fluid injection.

The problem at hand is quite original in the sense that it involves injection of a mean flow at the wall. In this case, the magnitude and the distance $y_{\max}$ from the wall to the point where maximum overshooting occurs can be determined numerically. The so-called Richardson effect[22] of a velocity overshoot is clearly observed in both analytical models to be much more intense than for the hardwall case.

Plots of velocity overshoot and loci of these velocity extrema are almost indistinguishable from corresponding numerical predictions. Note that the loci are independent of Re_k (i.e., viscosity), and only depend on Sr. For the regular perturbation model of $O(1/Sr)$,[7] numerical and analytical results become discernible when Sr drops below 20. Figure 5 summarizes the observed trends which, in turn, indicate that the overshoot increases with decreasing kinematic viscosity and frequency. As one would expect, the overshoot occurs in the vicinity of the wall, roughly, in the lower 25% of the solution domain, corresponding, indubitably, to the most sensitive region. Since this overshoot is not captured by the one-dimensional model currently in use, the need to incorporate the multidimensional field, described here, becomes even more important, especially when proper coupling with combustion is desired near the propellant surface.

Spatial Wavelength and Speed of Propagation

Near the wall, the speed of propagation of the vortical wave can be determined from

$$\left(k_m t+\Phi\right)\cong\left(k_m t-ySr\right)=2\pi j,\ j=1,2,\cdots \tag{6}$$

or, in dimensional form,

$$\left(\frac{m\pi a_0}{L}t^*-\frac{y^*}{R}Sr\right)=2\pi j \tag{7a}$$

$$a_w=\frac{dy^*}{dt^*}=\frac{1}{Sr}m\pi a_0\frac{R}{L}=V_b \tag{7b}$$

As expected, the speed of propagation near the wall is determined by the mean flow velocity. In a similar fashion, the dimensional wavelength of propagation can be calculated to be:

$$\lambda_w=\frac{a_w}{f_m}=2\pi\frac{a_w}{\omega_0}=\frac{2V_b}{ma_0}L \tag{8}$$

Away from the wall, the speed of propagation will not be a constant anymore. It will decrease with the radial mean flow velocity. Using the exact expression for the phase angle, the dimensional speed of propagation of the rotational wave in the radial direction is found to be exactly equal to the radial mean flow velocity:

$$a_w=\frac{dy^*}{dt^*}=\frac{1}{Sr}m\pi a_0\frac{r_0}{L}\left(\frac{r^*}{R}\right)^{-1}\sin\left(\frac{\pi}{2}\frac{r^*}{R}\right)=-V_bU_r \tag{9}$$

Having determined the speed of propagation, the spatial wavelength of rotational waves can be deduced easily. Written in nondimensional form, the result is

$$\frac{\lambda_w}{R}=2\pi\frac{a_w}{\omega_0 R}=-2\pi\frac{V_b}{\omega_0 R}U_r=-\frac{2\pi}{Sr}U_r \tag{10}$$

Clearly, the higher the Strouhal number, the shorter the wavelength, and the steeper the wave crests will be. Also, as the centerline is approached, the spatial wavelength diminishes in direct proportion with the radial mean flow velocity. This explains the larger number of reversals per unit of traveled distance for a fluid particle in approach of the centerline. The analytical expression for the spatial wavelength captures very accurately the physical details dictated in most part by Culick's mean flowfield.[24]

Unsteady Pressure Phase Lead

Here Φ is the phase angle of the vortical velocity component with respect to the acoustic counterpart at any radial position within the chamber. This function is proportional to Sr and controls the propagation speed of the rotational wave. The angle σ_m by which the sinusoidal time-dependent pressure wave leads the time-dependent velocity can be determined as follows. First, the time-dependent pressure and velocities are written as harmonic functions of time

$$\frac{p^{(1)}}{\varepsilon_w} = \cos(k_m t)\cos(k_m z) = \sin\left(k_m t + \frac{\pi}{2}\right)\cos(k_m z) \tag{11}$$

$$u^{(1)} = \frac{\varepsilon_w}{\gamma}\sqrt{(1 - A_m\cos\Phi)^2 + (A_m\sin\Phi)^2} \times \sin(k_m t + \beta_m)\sin(k_m z) \tag{12}$$

where, from Eq. (1),

$$\tan\beta_m = \frac{-A_m\sin\Phi}{1 - A_m\cos\Phi} \tag{13}$$

$$A_m = \sin\left(\frac{\pi}{2}r^2\right)\left[\sin(k_m z)\right]^{-1}\sin\left[k_m z\sin\left(\frac{\pi}{2}r^2\right)\right] \times \exp\left[\xi\eta(r)r^3\csc^3\left(\frac{\pi}{2}r^2\right)\right] \tag{14}$$

Then, for any axial location, the angle by which the pressure leads the velocity is simply

$$\sigma_m = \frac{\pi}{2} - \beta_m \tag{15}$$

Near the wall, the angle Φ is written in a Taylor series form expanded about $y = 0$:

$$\Phi(r) = \frac{Sr}{\pi}\ln\tan\left(\frac{\pi}{2}r^2\right) = \frac{Sr}{\pi}\left[-\pi y + \frac{\pi}{2}y^2 - \frac{\pi^3}{6}y^3 + \frac{\pi^3}{4}y^4 - \frac{(3+\pi^2)\pi^3}{24}y^5 + O(y^6)\right] \cong -ySr \tag{16}$$

The effective composite scale that appears in Eq. (14) also exhibits an asymptotic form near the wall.[2,3] At $y = 0$, the effective composite scale becomes

$$\eta(r) = -y \tag{17}$$

wherefore the vortical velocity amplitude given by Eq. (14) simplifies to

$$A_m = \exp[\xi\eta(r)] = \exp(-\xi y) \tag{18}$$

and the angle β_m, given by Eq. (13), becomes

$$\tan\beta_m = \left.\frac{-\exp(-\xi y)\sin(-ySr)}{1 - \exp(-\xi y)\cos(-ySr)}\right|_{y\to 0} = \frac{0}{0} \tag{19}$$

To remove the indeterminate character of Eq. (19), L'Hospital's rule is invoked. The result is a simple expression for the phase angle at the wall:

$$\lim_{y\to 0}\frac{\xi\exp(-\xi y)\sin(-ySr) + Sr\exp(-\xi y)\cos(-ySr)}{\xi\exp(-\xi y)\cos(-ySr) - Sr\exp(-\xi y)\sin(-ySr)} = \frac{Sr}{\xi} = SrS_p = \tan\beta_m \tag{20}$$

wherefrom

$$\beta_m = \arctan(SrS_p) \tag{21}$$

$$\sigma_m = \frac{\pi}{2} - \arctan(SrS_p) \tag{22}$$

This exact analytical limit is common to all rotational models, whether one-dimensional[1,4] or two-dimensional,[2,3,6,7] and whether using purely analytical means,[4] regular perturbations,[6,7] or multiple-scale techniques.[1,2,3] Additionally, this limit can be verified very rigorously by numerical computations. Near the centerline where acoustic velocity is the only nonzero component, the rotational velocity vanishes, β_m vanishes, and σ_m will be 90 degrees. Thusly, the sinusoidal time-dependent pressure leads the time-dependent velocity by an angle that varies from a small value at the wall to 90 degrees at the centerline. Not unlike the velocity profile, there exists a phase overshoot that can reach 180 degrees or twice the phase difference between pressure and acoustic velocity. At the wall, an exact analytical expression for the phase angle is successfully extracted. By inspection of Eq. (22), the phase angle depends on the product of the Strouhal number and the penetration number. In dimensional form, this product scales with the convection to diffusion speed ratio of the rotational disturbances introduced at the wall:

$$\sigma_m = \frac{\pi}{2} - \arctan\left(\frac{V_b^2}{\omega_0 \nu_0}\right) = \frac{\pi}{2} - \arctan\left(\frac{V_b^2 L}{m\pi a_0 \nu_0}\right) \tag{23}$$

It follows that lower injections, shorter chambers, higher oscillation modes, higher viscosities, or higher speeds of sound result in a larger pressure to velocity phase lead at the wall. The largest phase lead will occur, for instance, in a small SRM. Practically, this angle is only a few degrees or less. Figure 6 shows the phase lead of the time-dependent pressure with respect to the velocity for the four typical cases defined in Ref. 6, using two-dimensional viscous[3,7] and inviscid formulations,[6] in addition to the one-dimensional near-wall solution from Ref. 4. At the wall, the exact expression for the phase angle given by Eq. (23) is verified to be common to all three models.

Practical Boundary-Layer Equation

In order for the analytical models to match corresponding numerical predictions, it is not necessary to retain all the terms in the rotational momentum equation that controls the character of the oscillatory boundary layer. In reality, of all the terms appearing in the momentum equation given as Eq. (9) in Ref. 3,

$$\frac{\partial \tilde{u}_z}{\partial t} = -\frac{k_m}{Sr}\left[\frac{\partial}{\partial z}\left(\tilde{u}_z U_z\right) + U_r \frac{\partial \tilde{u}_z}{\partial r} + \tilde{u}_r \frac{\partial U_z}{\partial r}\right] + \frac{k_m}{Re_k}\left(\frac{\partial^2 \tilde{u}_z}{\partial r^2} + \frac{1}{r}\frac{\partial \tilde{u}_z}{\partial r} - \frac{1}{r}\frac{\partial \tilde{u}_r}{\partial z} - \frac{\partial^2 \tilde{u}_r}{\partial r \partial z}\right) \tag{24}$$

only five significant terms need to be retained:

$$\frac{\partial \tilde{u}_z}{\partial t} = -\frac{k_m}{Sr}\left(U_r \frac{\partial \tilde{u}_z}{\partial r} + U_z \frac{\partial \tilde{u}_z}{\partial z} + \tilde{u}_z \frac{\partial U_z}{\partial z}\right) + \frac{k_m}{Re_k}\frac{\partial^2 \tilde{u}_z}{\partial r^2} \tag{25}$$

These terms contribute to the solution in both models and can be attributed to five physical mechanisms. All the remaining terms in Eq. (24) may be included, but the corrections that will result in retaining them will be smaller than the order of the error in the solution itself. As can be established by tracking the leading order terms that influence the solution, the most important physical mechanisms can be associated with unsteady inertial forces and both radial and axial convection of unsteady vorticity by the mean flow. Second in importance is the viscous diffusion of vorticity. Third in importance is the convective coupling between unsteady velocity and mean flow vorticity. It is the balance of these important physical phenomena that controls the oscillatory motion of gases inside the chamber. In essence, Eq. (25) is the practical, "real world," time-dependent boundary-layer equation.

Comparisons to Computational Predictions

Previously in Ref. 3, analytical results were shown to be in fair agreement with experimental observations made by other researchers. Presently, comparisons will be made against a reliable numerical code developed totally independently by Roh and co-workers.[23] Sometimes referred to as the "dual time-stepping" (DTS) code, this compressible Navier-Stokes solver has recently received wide acceptance in the combustion stability community by virtue of its established accuracy and reliability.

On that account, DTS data (shown in dashed lines) are compared in Fig. 7 to analytical predictions (shown in solid lines) at approximately the same time intervals for a typical case of a cylindrical chamber ($L = 2.03$ m, $R = 0.102$ m). The injection speed is held constant at 1.02 m/s (corresponding to a Mach number of 0.003), and the kinematic viscosity is taken to be 2.61×10^{-5} m^2/s. The corresponding dynamic similarity parameters are calculated to be $Re_k = 2.1 \times 10^5 m$, $Sr = 52.6m$, and $S_p = 1.44/m^2$.

As shown in Fig. 7, there is a good agreement between computational and analytical predictions for velocity amplitudes and spatial wavelengths near the wall. A strong resemblance in the general structure of the boundary layer may be said to exist at higher oscillation modes, as shown in

Figs. 7b-c. In particular, both approaches predict the occurrence of m points of zero rotational wave amplitude at the m^{th} velocity antinode attributed to the downstream convection of zero vorticity lines by the bulk fluid motion. These comparisons were limited to the first two acoustic modes due to the rapidly increasing cost of achieving numerical solutions at higher modes.

The slight deviation of DTS data from analytical predictions can be attributed to unavoidable limitations in available computational power. In reality, several sources of numerical uncertainties have been identified as possible reasons for the observed discrepancy.[28]

First, due to memory resource limitations, it becomes unaffordable to refine the grid sufficiently enough in regions that are distant from the wall where the mean radial velocity becomes very small. The reason for using very fine grid spacing is necessitated by the need to properly resolve the vorticity wave whose wavelength depends directly on the mean radial velocity. The analytical model does not suffer from this limitation and, as shown in Fig. 7, is capable of resolving very precisely the spatial wavelength away from the wall even when the mean velocity becomes infinitesimally small. In light of this argument, a progressive deviation from analytical predictions is to be anticipated as the distance from the wall is increased, when a slight deterioration in numerical accuracy becomes unavoidable.

Second, due to the numerical inability to match exactly the time intervals required for comparisons during a cycle (i.e., $\pi/2$, π, and $3\pi/2$), which happen to be irrational numbers, numerical data is acquired at time intervals that are closest to the times desired. This restriction in the numerical approach is caused by the need for finite time discretization and is obviated in analytical formulations. In the current analysis, the time period was divided into 100 time steps, making it difficult to match the prescribed time intervals which, evidently, brings in additional errors to DTS data. This explains the slight asymmetry in the numerically generated curves, and their subtle deviation from analytical curves away from the wall, in the fully irrotational zone.

Third, due to the reliance of numerical calculations on artificial dissipation, it can become difficult to refine the artificial dissipation sufficiently enough. Needless to say, analytical models are not dependent on artificial dissipation.

Reducing numerical errors, which is expected to improve substantially the agreement with analytical predictions, can be accomplished through 1) decreasing artificial dissipation in the numerical scheme, 2) refining the grid, and 3) decreasing each time step. Unfortunately, these improvements can only be implemented at the expense of increased computational time, cost, and memory allocation which, collectively, can become prohibitive. In conclusion, the analytical models described heretofore, being exempt from computational setbacks, appear to capture the key physical details furnished by the DTS procedure, for the laminar case, while remaining immune to numerical restrictions.

Impact and Implications

The unsteady boundary layer in oscillatory flows with sidewall injection is an interesting addition to boundary-layer theory in fluid mechanics. It is also of value in the studies of turbulence in oscillatory flows over transpiring surfaces. Fortuitously, this solution can be verified analytically to be rigorous since it reduces to Sexl's solution[26] near the wall in the limit of a very small injection velocity (to be addressed in our forthcoming work). In rocket dynamics, it furnishes a simple yet powerful expression capable of elucidating the intricate features of the acoustic boundary layer whose structure has been the subject of much controversy in the past.

Importance in Fluid Mechanics

A multidimensional analytical solution that quantifies the Stokes boundary layer in an oscillatory duct flow with sidewall injection is exploited here including the axial dependence. It appears that this analytical solution, along with Flandro's model,[7] are the only two-dimensional axisymmetric expressions pertaining to this type of flow which have been obtained so far. Both offer important steps aimed at a more complete understanding of the structure of the Stokes layer over porous surfaces. Such understanding may be needed to allow improved formulations in aerodynamics, gas dynamics, studies of blood flow in arteries, and other applications. In the studies of turbulence, the availability of a laminar solution can be used as a basis for investigating turbulent behavior, which, up to this time, is not very well understood. Both experimental and numerical studies of turbulence in oscillatory duct flows with sidewall injection can benefit from a closed form solution of the internal flowfield as furnished here. The analytical methodology itself may be applicable to similar physical settings involving oscillatory flows.

Importance in Rocket Dynamics

The existence of an accurate, yet simple, analytical expression for the unsteady flow component has a major impact on the internal flowfield modeling strategy and combustion stability assessment in solid rocket motors. The current standard prediction model that is used to analyze combustion stability of various rockets assumes the existence of a one-dimensional irrotational component of the time-dependent flow and introduces patches to account for three-dimensional effects. The current analysis emphasizes the importance of the rotational flow component in altering the boundary layer character. Evidently, the actual structure of the boundary layer is quite different from the "thin" acoustic layer assumed in one-dimensional models. By analogy to Culick's steady flow solution,[7] the present unsteady solution could be incorporated into existing codes and models to improve prediction capabilities. Other mechanisms that are associated with combustion instability could also be revisited in light of this new model. For example, the flow turning loss that is used as a corrective term to patch the one-dimensional imperfection of the model can be shown to be no longer necessary.[7] Flandro has actually shown that, when his formulation is used,[7] a term will appear —in the resulting solution— that is identical to the flow turning loss; the latter being artificially added to the one-dimensional solution. In other areas, the velocity coupling phenomenon can be quite possibly improved by incorporating an accurate, yet simple formulation of the time-dependent velocity field. The same can be said of studies involving particulate damping, acoustic streaming, acoustic admittance, erosive burning, turbulence, etc..

Importance of a New Similarity Parameter

By analogy to the Stokes number that governs the thickness of the boundary layer in oscillating flows with inert walls, the penetration number is found to play a similar role in the case when the walls are made porous. This number

$$S_p = \frac{1}{\xi} = \frac{V_b^3}{\omega_0^2 \nu_0 R} \tag{26}$$

explains what other researchers[1-9] have noticed before; namely, that the thickness of the boundary layer will depend mostly on the injection velocity (being elevated to the third power). The frequency of oscillations is the second most important parameter. Doubling the frequency of oscillations decreases the penetration number by a factor of four, which, at sufficiently high frequencies, reduces the boundary-layer thickness by a factor of four also (since the penetration number and the penetration depth are directly proportional in the lower portion of the domain, regardless of axial position). The role of viscosity is finally established as an attenuation factor. This is due to the fact that the penetration number is inversely proportional to the kinematic viscosity. In contrast to steady boundary layers, or to Stokes boundary layers in oscillatory flows with imporous walls, the role of viscosity when injection is included is to attenuate rather than promote the growth of the boundary layer. The penetration depth is found to be a measure of the rotational region of the flow. Physically, oscillatory vorticity is constantly generated at the wall as a result of the oscillatory pressure gradient which is parallel to the solid boundary at the injection surface. Due to the mean flow motion, vorticity is convected inwardly in an attempt to contaminate the irrotational fluid with vorticity. The growth of the vortical region results from the convection and diffusion of vorticity into the inner regions of the domain where convective, diffusive, and inertial acceleration effects stand balanced. The amplitude of the oscillatory vorticity will cease to change when viscous dissipation and downstream convection of vorticity manage to annihilate the radial propagation effects. The edge of the boundary layer is hence recognized as a point that is located at a distance y_p from the wall, above which the propagation of vorticity is negligible. The flowfield above this depth of penetration can be said to be irrotational. The boundary-layer region is, in the context described here, a region of highly concentrated vorticity. Finally, the chamber geometry appears to have a direct effect on the penetration number also. Decreasing the motor's effective radius causes the penetration depth to grow proportionately larger. This is to be expected because the effect of blowing becomes more appreciable when the cross-sectional area is reduced.

Conclusions

The classical concepts of boundary-layer theory regarding inner, near-wall, and outer, external regions are almost reversed for the case of an unsteady flow over a transpiring surface. Near the wall, instead of observing the thin, inner, viscous layer as in unsteady Stokes or steady flows, a thick rotational layer is established near the solid boundary when sidewall injection is incorporated because of vorticity convection in the radial direction. The penetration depth is simply a measure of the vortical region. The thin layer where viscous friction is important is removed from the wall to the edge of the Stokes boundary layer. The penetration depth is a direct function of a similarity number that is proportional to the cube of the injection speed, inversely proportional to the square of the frequency, and inversely proportional to the viscosity and chamber effective radius. This dependence is in total agreement with empirical observations as well as numerical analyses. Accordingly, the role of viscous diffusion is to attenuate the amplitude of shear waves and to reduce the depth of penetration. The role of frequency is similar to viscosity, only twice as important. Injection velocity is the most important variable affecting the boundary-layer thickness. Higher combustion temperatures in rockets lead to higher kinematic viscosities and, therefore, to smaller penetration numbers. Higher oscillation modes (and, therefore, frequencies) have a similar effect. The axial location in the chamber also affects the boundary-layer thickness depending on the acoustic mode. The role of the Strouhal number as the controlling parameter for the vortical-to-acoustical phase angle has been elucidated. The current analysis clearly shows that increasing the Strouhal number steepens the vortical wave crest and reduces its wavelength. The pressure-to-velocity phase at the wall is found to be controlled by the ratio of the convection-to-diffusion speed of the vortical waves.

The key elements defining the structure of the boundary layer are accurately captured by the CST solution which, unlike computational predictions, does not suffer from limitations imposed on grid resolution, time discretization size, artificial dissipation, and so forth. It is hoped that this technique be further explored in related combustion stability research, taking advantage of the scaling synthesis verified to be accurate in this investigation, and which can be particularly useful in pursuing models for turbulence. Analytical development of a turbulent flow model can now evolve from the established knowledge of similarity parameters and agents in control of the laminar boundary layer.

Acknowledgments

The author is indebted to Prof. Vigor Yang and his co-workers from Pennsylvania State University for their generous contribution of DTS data that made analytical comparisons to nonlinearized, compressible Navier-Stokes predictions possible.

References

[1] Majdalani, J., and Van Moorhem, W.K., "The Unsteady Boundary Layer in Solid Rocket Motors," Paper No. AIAA-95-2731, July 1995.

[2] Majdalani, J., and Van Moorhem, W.K., "A Multiple-Scales Solution to the Acoustic Boundary Layer in Solid Rocket Motors," *Journal of Propulsion and Power*, Vol. 13, No. 2, 1997, pp. 186-193.

[3] Majdalani, J., and Van Moorhem, W.K., "An Improved Time-Dependent Flowfield Solution for Solid Rocket Motors," *AIAA Journal*, Vol. 36, No. 2, 1998, pp. 241-248.

[4] Flandro, G.A., "Effects of Vorticity Transport on Axial Acoustic Waves in a Solid Propellant Rocket Chamber," *Combustion Instabilities Driven By Thermo-Chemical Acoustic Sources*,

NCA Vol. 4, HTD Vol. 128, American Society of Mechanical Engineers, New York, 1989.

[5] Smith, T.M., Roach, R.L., and Flandro, G.A., "Numerical Study of the Unsteady Flow in a Simulated Rocket Motor," AIAA Paper 93-0112, Jan. 1993.

[6] Flandro, G.A., "Effects of Vorticity on Rocket Combustion Stability," *Journal of Propulsion and Power*, Vol. 11, No. 4, 1995, pp. 607-625.

[7] Flandro, G.A., "On Flow Turning," AIAA Paper 95-2730, July 1995.

[8] Beddini, R.A., and Roberts, T.A., "Response of Propellant Combustion to a Turbulent Acoustic Boundary Layer," AIAA Paper 88-2942, July 1988.

[9] Beddini, R.A., and Roberts, T.A., "Turbularization of an Acoustic Boundary-Layer on a Transpiring Surface," AIAA Paper 86-1448, June 1986.

[10] Sabnis, J.S., Giebeling, H.J., and McDonald, H., "Navier-Stokes Analysis of Solid Propellant Rocket Motor Internal Flows, *Journal of Propulsion and Power*, Vol. 5, No. 6, 1989, pp. 657-664.

[11] Tissier, P.Y., Godfrey, F., Jacquemin, P., "Simulation of Three Dimensional Flows Inside Solid Propellant Rocket Motors Using a Second Order Finite Volume Method – Application to the Study of Unstable Phenomena," AIAA Paper 92-3275, July 1992.

[12] Vuillot, F. and Avalon, G., "Acoustic Boundary Layer in Large Solid Propellant Rocket Motors Using Navier-Stokes Equations," *Journal of Propulsion and Power*, Vol. 7, No. 2, 1991, pp. 231-239.

[13] Vuillot, F. Lupoglazoff, N., "Combustion and Turbulent Flow Effects in 2D Unsteady Navier-Stokes Simulations of Oscillatory Rocket Motors", AIAA Paper 96-0884, Jan. 1996.

[14] Vuillot, F., "Acoustic Mode Determination in Solid Rocket Motor Stability Analysis," *Journal of Propulsion and Power*, Vol. 3, No. 4, 1987, pp. 381-384.

[15] Vuillot, F., "Numerical Computation of Acoustic Boundary Layers in a Large Solid Propellant Space Booster," AIAA Paper 91-0206, Jan. 1991.

[16] Vuillot, F., "Numerical Computation of Acoustic Boundary Layers in Large Solid Propellant Space Booster," AIAA Paper 91-0206, Jan. 1991.

[17] Vuillot, F., and Avalon, G., "Acoustic Boundary Layer in Large Solid Propellant Rocket Motors Using Navier-Stokes Equations," *Journal of Propulsion and Power*, Vol. 7, No. 2, 1991, pp. 231-239.

[18] Vuillot, F., Avalon, G. "Acoustic Boundary Layers in Solid Propellant Rocket Motors Using Navier-Stokes Equations," *Journal of Propulsion and Power*, Vol. 7, No. 2, 1991, pp. 231-239.

[19] Vuillot, F., Dupays, J., Lupoglazoff, N., Basset, Th., and Daniel, E., "2D Navier-Stokes Stability Computations for Solid Rocket Motors: Rotational, Combustion and Two-Phase Flow Effects," AIAA Paper 97-3326, July 1997.

[20] Roberts, T.A. and Beddini, R.A., "Response of Solid Propellant Combustion to the Presence of a Turbulent Acoustic Boundary Layer," AIAA Paper 88-2942, July 1988.

[21] Shaeffer, C.W., and Brown, R.S., "Oscillatory Internal Flow Studies," Chemical Systems Div., Rept. 2060 FR, United Technologies, San Jose, CA, Aug. 1992.

[22] Richardson, E. G., "The Amplitude of Sound Waves in Resonators," *Proceedings of the Physical Society, London*, Vol. 40, Dec. 1937-Aug. 1928, pp. 206-220.

[23] Roh, T.S., Tseng, I.S., and Yang, V., "Effects of Acoustic Oscillations on Flame Dynamics of Homogeneous Propellants in Rocket Motors," *Journal of Propulsion and Power*, Vol. 11, No. 4, July 1995, pp. 640-650.

[24] Culick, F.E.C., "Rotational Axisymmetric Mean Flow and Damping of Acoustic Waves in Solid Propellant Rocket," *AIAA Journal,* Vol. 4, No. 8, 1966, pp. 1462-1464.

[25] Butcher, J.C., "On Runge-Kutta Processes of Higher Order," *Journal of the Australian Mathematical Society*, Vol. 4, 1964, pp. 179-194.

[26] Sexl, T., "Über den von E.G. Richardson entdeckten 'Annulareffekt'," *Zeitschrift für Physik*, Vol. 61, 1930, pp. 349-362.

[27] Richardson, E.G., and Tyler, E., "The Transverse Velocity Gradient Near the Mouths of Pipes in Which an Alternating or Continuous Flow of Air Is Established," *Proceedings of the Physical Society, London*, Vol. 42, 1929, pp. 1-15.

[28] Through personal communication with W. Cai from Pennsylvania State University.

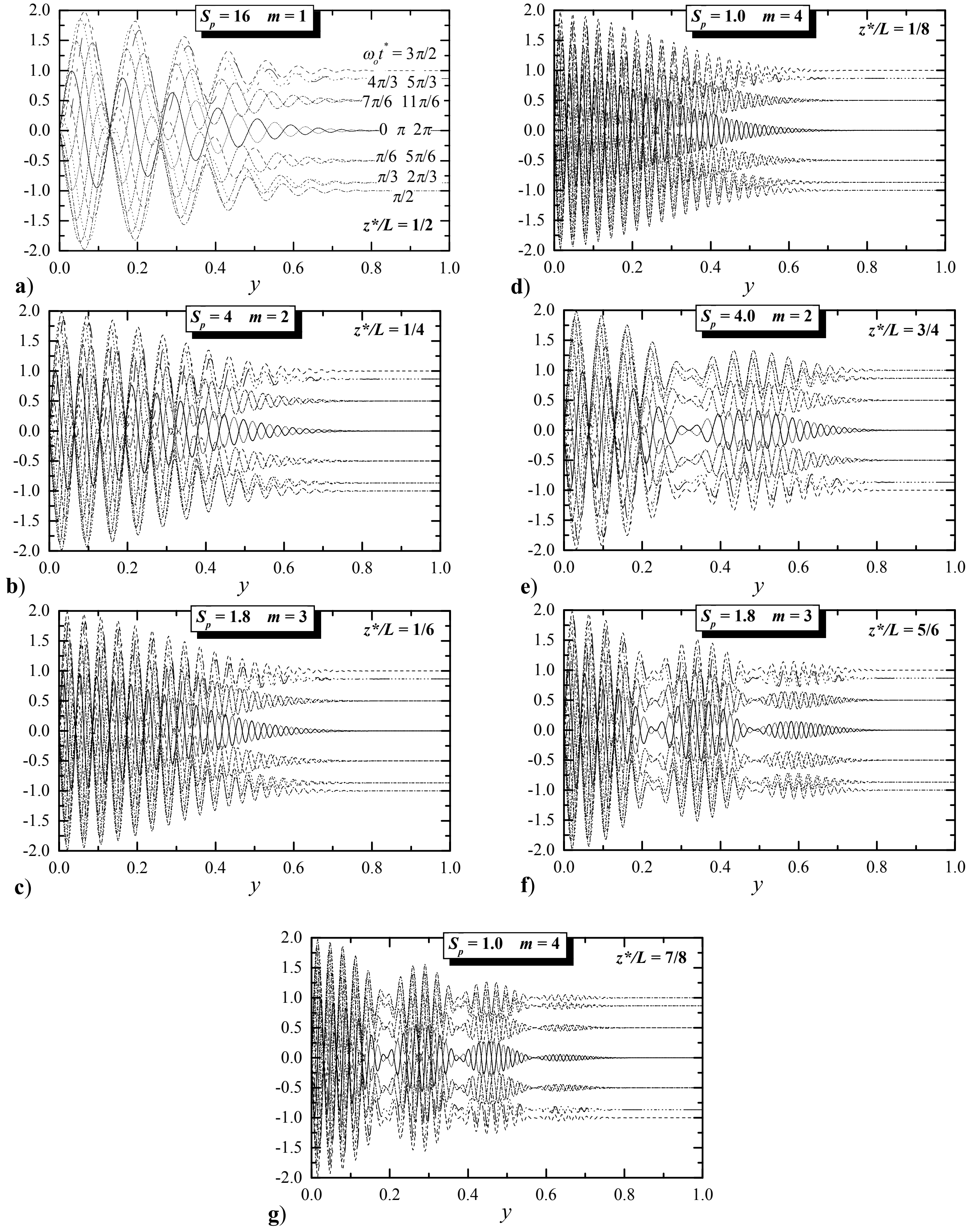

Fig. 1 Velocity evolutions from numerical, regular perturbations,[7] and CST[3] models shown at 13 evenly spaced times in a typical tactical rocket motor for the first 4 acoustic modes at the first (a-d) and last (e-g) acoustic velocity antinode.

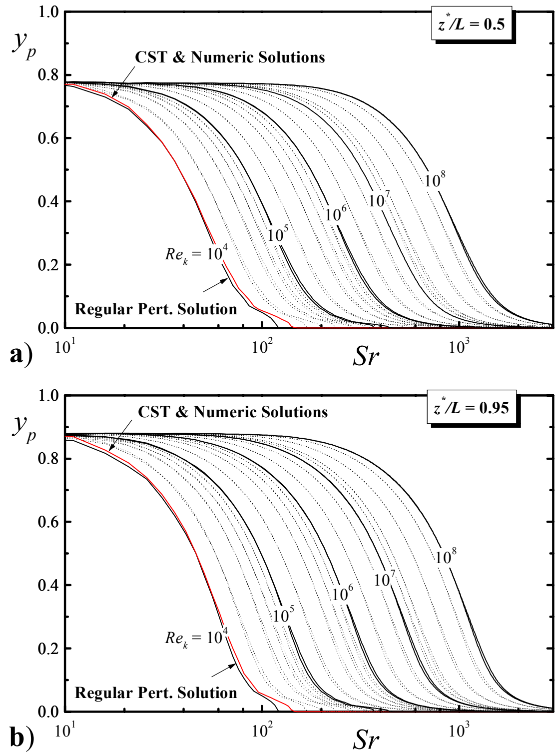

Fig. 2 Penetration depths obtained numerically and from two analytical models[3,7] for a wide range of control parameters and two axial locations.

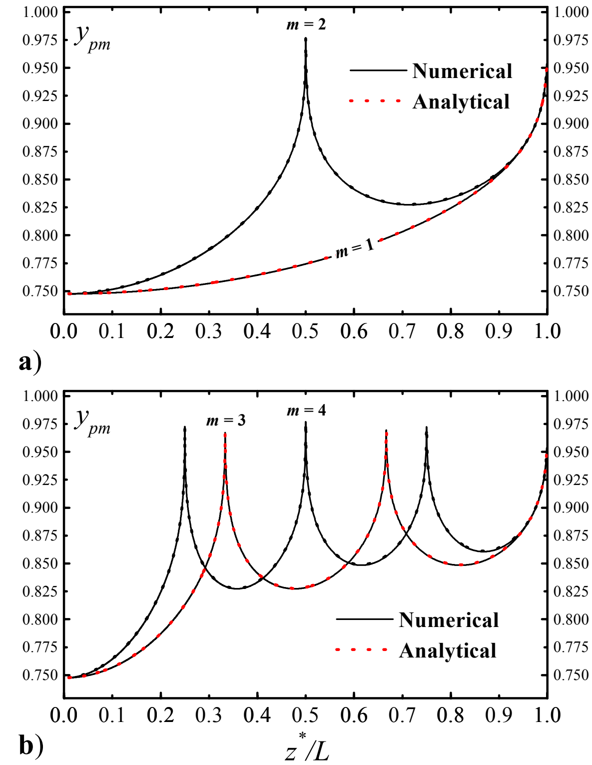

Fig. 4 Trace of the maximum boundary-layer thickness for the first four acoustic modes: (a) $m = 1$, 2 and (b) $m = 3$, 4.

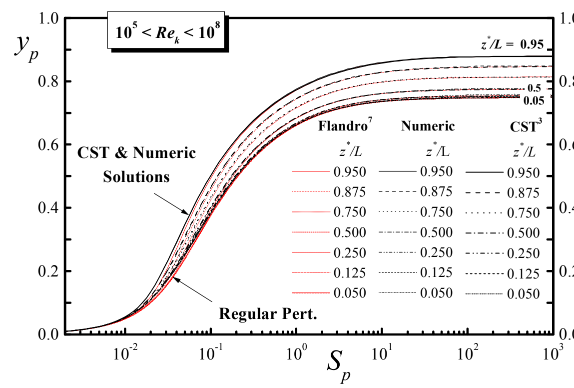

Fig. 3 Locus of the boundary-layer thickness obtained numerically and from two analytical models[3,7] for a vast range of control parameters at various axial locations.

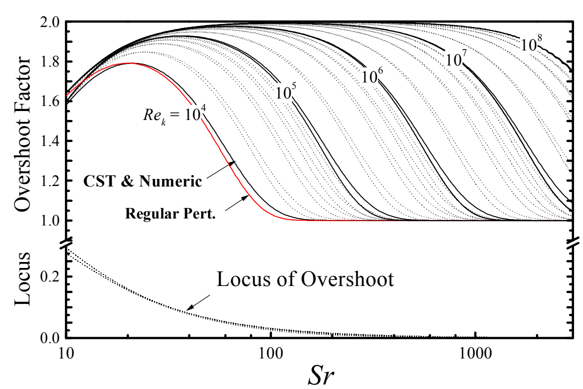

Fig. 5 Analytical and numerical predictions for the locus and magnitude of Richardson's velocity overshoot at $z^* = 0.5L$ and a wide range of control parameters.

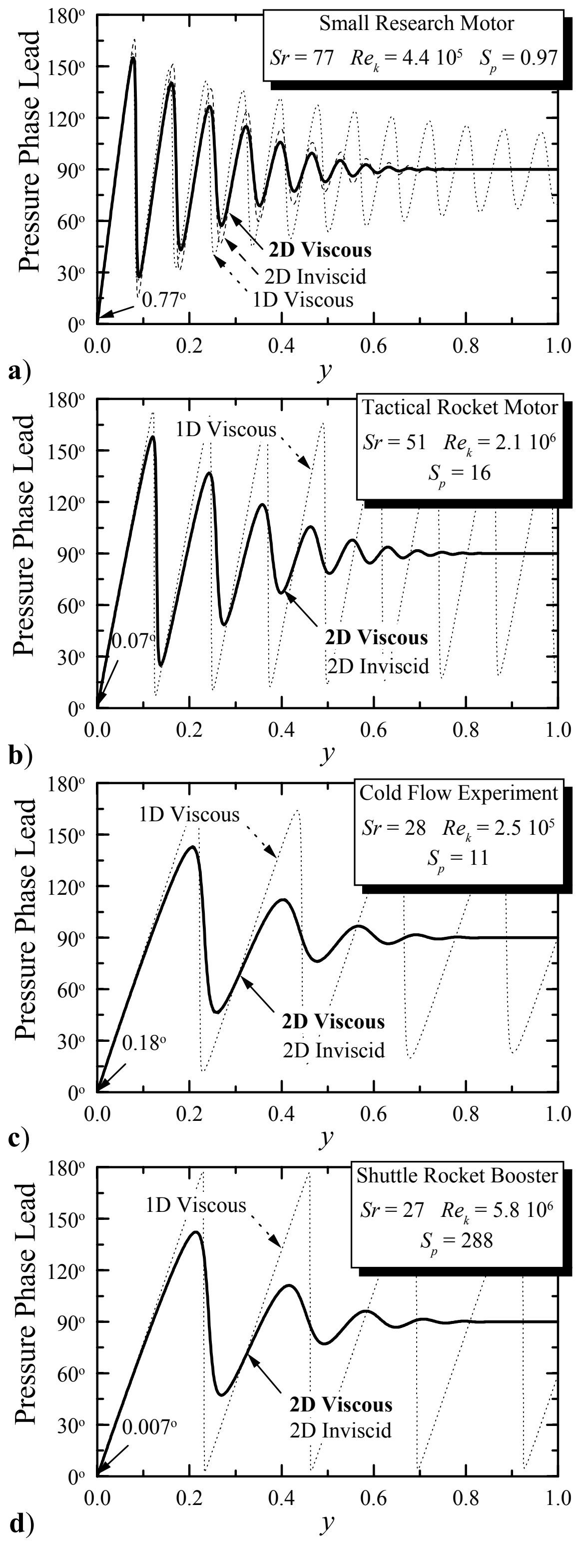

Fig. 6 Unsteady pressure to velocity phase lead using CST,[3] regular perturbations, viscous[7] and inviscid[6] models, and the one-dimensional model,[4] all at m = 1 and chamber midlength; the four typical cases span the range of solid rocket motors.

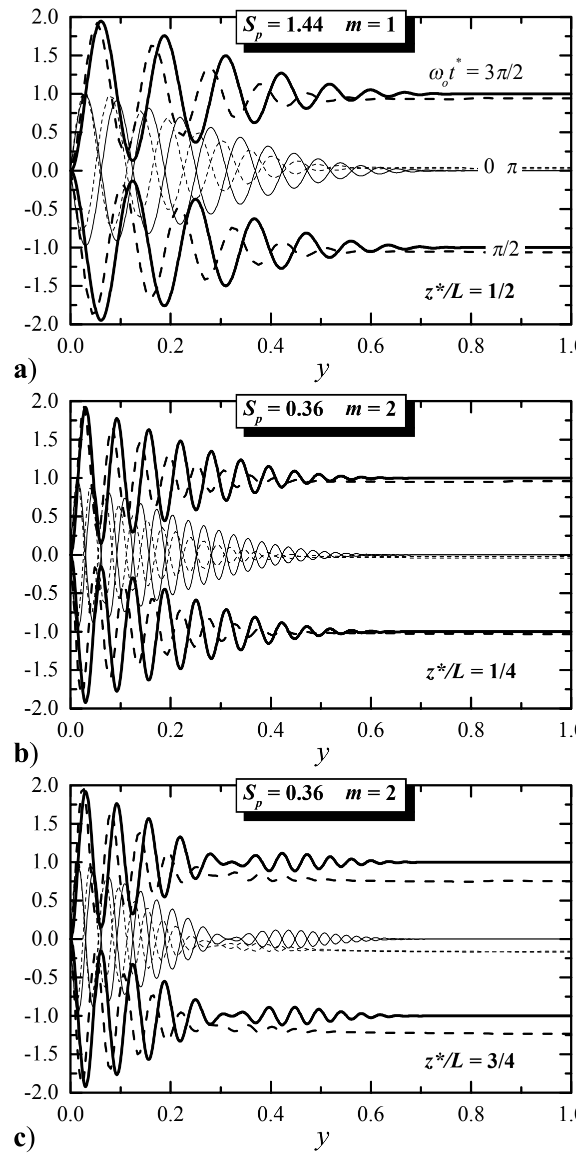

Fig. 7 Comparison of time-dependent velocity evolutions at 4 evenly spaced times acquired from analytical predictions[3] (shown by solid lines) and Navier-Stokes data[23] (shown by dashed lines) for the first 2 modes of oscillations evaluated at the axial location of the first (a-b) and last (c) acoustic velocity antinode.